Gliding motility of *Plasmodium* merozoites

Kazuhide Yahata[a,b,1,*], Melissa N. Hart[c,1], Heledd Davies[b], Masahito Asada[a,d], Samuel C. Wassmer[c], Thomas J. Templeton[a], Moritz Treeck[b], Robert W. Moon[c,*], Osamu Kaneko[a]

[a]Department of Protozoology, Institute of Tropical Medicine (NEKKEN), Nagasaki University, Nagasaki, Japan

[b]Signalling in Apicomplexan Parasites Laboratory, The Francis Crick Institute, London, UK

[c]Faculty of Infectious and Tropical Diseases, London School of Hygiene & Tropical Medicine, London, UK

[d]National Research Center for Protozoan Diseases, Obihiro University of Agriculture and Veterinary Medicine, Obihiro, Hokkaido, Japan

[1]These authors contributed equally

*Correspondence: kyahata@nagasaki-u.ac.jp or rob.moon@lshtm.ac.uk

Abstract

Plasmodium malaria parasites are obligate intracellular protozoans that use a unique form of locomotion, termed gliding motility, to move through host tissues and invade cells. The process is substrate-dependent and powered by an actomyosin motor that drives the posterior translocation of extracellular adhesins which in turn propel the parasite forward. Gliding motility is essential for tissue translocation in the sporozoite and ookinete stages; however, the short-lived erythrocyte-invading merozoite stage

has never been observed to undergo gliding movement. Here we show *Plasmodium* merozoites possess the ability to undergo gliding motility and that this mechanism is likely an important precursor step for successful parasite invasion. We demonstrate that two human infective species, *P. falciparum* and *P. knowlesi*, have distinct merozoite motility profiles which may reflect distinct invasion strategies. Additionally, we develop and validate a higher throughput assay to evaluate the effects of genetic and pharmacological perturbations on both the molecular motor and complex signaling cascade that regulates motility in merozoites. The discovery of merozoite motility provides a new model to study the glideosome and may facilitate the pursuit of new targets for malaria treatment.

Significance statement

Plasmodium malaria parasites use a unique substrate-dependent locomotion termed gliding motility to translocate through tissues and invade cells. Dogma has suggested that the small labile invasive stages that invade erythrocytes, merozoites, use this motility solely to penetrate target erythrocytes. Here we reveal that merozoites use gliding motility for translocation across host cells prior to invasion. This forms an important pre-invasion step that is powered by a conserved actomyosin motor and is regulated by a complex signaling pathway. This work fundamentally changes our understanding of the role of gliding motility and invasion in the blood and will have a significant impact on our understanding of blood stage host-pathogen interactions, parasite biology, and could have implications for vaccine development.

Introduction

Apicomplexan parasites traverse tissues and invade cells via a mechanism known as gliding motility, a process unique to the phylum that uses neither propulsive structures such as flagella or cilia, nor cellular shape changes as for peristaltic and amoeboid motility (1, 2). Motility of invasive forms of malarial parasites (termed "zoites") was first described for the ookinete stage in avian blood (3), and then for the sporozoite stage in the mosquito (4, 5). Unlike ookinetes and sporozoites, which must traverse through tissues, no gliding motility has been described for the merozoite, which invades erythrocytes in the bloodstream. Instead, only limited reorientation movement and cellular deformation has been observed across several malarial parasite species, including *Plasmodium knowlesi*, *P. falciparum,* and *P. yoelii* (6-8). Due to frequent and passive encounters with erythrocytes in the bloodstream shortly after egress, it has been presumed that merozoites do not require motility, leading to the consensus that the molecular motor is principally required for entry into the erythrocyte (9).

Gliding has perhaps been best described for *Toxoplasma gondii* tachyzoites and *Plasmodium berghei* sporozoites, both of which exhibit helical motion in 3D matrices, as well as during host cell entry (10-12). Treatment of tachyzoites and sporozoites with either cytochalasin D, an inhibitor of actin polymerization, or butanedione monoxime, a myosin inhibitor, stalls both extracellular motility and host cell invasion, indicating that both processes are driven by an actomyosin-based motor (7). Subsequent work discovered that the components of this motor, collectively called the “glideosome”, are located within the space between the parasite inner membrane complex (IMC) and plasma membrane; and are generally conserved between apicomplexan zoites, including merozoites (11, 13, 14). According to the linear motor model, gliding is a substrate-dependent process. Transmembrane ligands are

75 secreted from organelles called micronemes at the apical end of the zoite, where they
76 bind to receptors on the surface of the host cell or tissue via their ectodomains, whilst
77 also connecting to the actomyosin motor through their cytoplasmic tails (11). MyoA
78 engagement with actin subsequently pulls both actin and the receptor-bound ligand
79 rearward, thereby driving the zoite forwards. Finally, the ectodomains of receptor-
80 bound ligands are cleaved by parasite-derived proteases, thus disengaging them from
81 their host cell receptors (11). Deletion of key motor components, including myosin A
82 (MyoA) (15), actin-1 (ACT1) (16), and glideosome-associated protein 45 (GAP45)
83 (17), prevent *P. falciparum* merozoites from invading host erythrocytes, demonstrating
84 the essentiality of the actomyosin motor for erythrocyte invasion (9).

85 Here we show that both *P. falciparum* and *P. knowlesi* merozoites are capable
86 of gliding motility across both erythrocyte surfaces and polymer coverslips. Distinctive
87 gliding dynamics are found between the two species, suggesting that motility
88 modulates multiple steps of invasion. We developed an assay to evaluate the effect of
89 genetic and pharmacological perturbations on both the molecular motor and complex
90 signaling cascade that regulates motility in merozoites.
91

Results

Gliding motility of *Plasmodium* merozoites

Here we sought to address the long-standing dogma that malarial merozoites do not undergo conventional gliding motility. Whilst motility of sporozoites is normally observed on bovine serum albumin-coated glass slides, merozoites do not glide on this substrate. However, when using polymer coverslips with a hydrophilic coating (ibiTreat), we observed motile merozoites. When imaged immediately after erythrocyte egress, *P. falciparum* merozoites show directional movement on the coverslip surface which displaces them from the hemozoin-containing residual body (Fig. 1*A* and *B*; *SI Appendix,* Movies S*1* and *2*). The average *P. falciparum* merozoite gliding speed was 0.59 μm/second (SD = 0.14 μm/second; n = 10 individual merozoites), considerably slower than that of *P. yoelii* sporozoites (helical gliding 5.02 μm/second; SD = 0.83 μm/second; n = 8), *Toxoplasma gondii* tachyzoites (helical gliding 2.60 μm/second; SD = 0.54 μm/second; n = 13; circular gliding 1.84 μm/second; SD = 0.32 μm/second; n = 13), and *Babesia bovis* merozoites (6.02 μm/second; SD = 0.73 μm/second; n = 5), but significantly faster than *P. berghei* ookinetes (helical gliding 5.8 μm/min) (18). The longest gliding time of *P. falciparum* merozoites was 43 seconds, shorter than those of *P. yoelii* sporozoites (> 600 seconds), *T. gondii* tachyzoites (> 600 seconds) and *B. bovis* merozoites (125 seconds). Thus, the short-lived motility of *P. falciparum* merozoites appears to correlate with their decline in erythrocyte invasion efficiency within a few minutes after egress (19).

The zoonotic malaria parasite, *P. knowlesi,* has much larger and longer-lived merozoites (19-21) and is capable of invading both human and macaque erythrocytes (22); thus, we hypothesized that this may result in different gliding behavior. In the absence of fresh erythrocytes, *P. knowlesi* merozoites also exhibit some motility on

117 ibiTreat coverslips, but the number of motile merozoites increases using poly-L-lysine-
118 coated (PLL) polymer coverslip surfaces (*SI Appendix,* Movie S3). A median 62% (IQR
119 = 55%) of all merozoites within a given schizont exhibited motility on PLL-coated
120 coverslips, with a 'gliding' merozoite defined as one which attached to the coverslip
121 surface and exhibited forward movement for at least 5 continuous seconds (Fig. 2*A*).
122 To test whether gliding is surface dependent, *P. knowlesi* merozoites were also
123 monitored on uncoated polymer and glass coverslips. A much lower percentage of
124 motile parasites was observed for the uncoated polymer (mean = 38%; SD = 36%)
125 and glass coverslips (mean = 25%; SD = 22%) (*SI Appendix,* Fig. S1*A*). This suggests
126 that both the coating and the use of polymer rather than glass coverslips is critical for
127 optimal gliding to occur and may account for why merozoite motility has not been
128 observed previously.

129 *P. knowlesi* merozoites were faster (mean = 1.06 μm/second; SD = 0.29
130 μm/second; n = 57 individual merozoites) than *P. falciparum* (*SI Appendix,* Fig. S1*B*)
131 and were capable of gliding for up to 316 seconds (Fig. 2*B*) on PLL surfaces. To
132 assess the involvement of an actomyosin motor for merozoite motility, egressing
133 merozoites were treated with the actin polymerization inhibitor, cytochalasin D (0.1
134 μM; IC_{50} = 23 nM). This treatment completely inhibited motility (Fig. 2*A* and *SI*
135 *Appendix,* Movie S4). Cytochalasin D addition also prevented efficient dispersal post
136 egress and frequently resulted in merozoites remaining attached to each other and/or
137 the residual body (Fig. 2*A* and *SI Appendix,* Movie S4). However, whilst dispersal was
138 inhibited, cytochalasin D treatment did not impede egress itself, as visualized using
139 wheatgerm agglutinin-stained erythrocytes and *P. knowlesi* schizonts treated with the
140 drug (*SI Appendix,* Movie S4). The capacity for erythrocyte egress is in line with
141 observations of cytochalasin D-treated *P. falciparum* parasites (17) (*SI Appendix,*

Movie S4). Even without inhibitors, *P. knowlesi* merozoite movement was sometimes impaired by groups of merozoites remaining attached to each other. Notably, though, in many instances, pairs, or smaller groups of merozoites were frequently observed to glide together in unison, when “pointing” in the same direction. Merozoites often completed several glides, with a median cumulative distance of 14 μm (IQR =16 μm), and some travelling as far as 200 μm within the 10-minute imaging window (*SI Appendix,* Fig. S1*D*). The majority of gliding occurred within 5 minutes of egress (*SI Appendix,* Fig. S1*E*), with peak gliding occurring during the initial 1 to 2 minute window. Gliding speed appeared to decline over subsequent glides (*SI Appendix,* Fig. S1*F*), indicative of declining motor function over time, which potentially contributes to the window of merozoite viability. No increase in gliding activity was observed when freshly egressed parasites were first incubated in the dark for 5 minutes prior to commencing imaging for an additional 4 minutes (SI Appendix, Fig. S1*E*). Thus, for *P. knowlesi*, continuous light exposure is unlikely to be the cause of declining motor function (*SI Appendix*, Fig. S1*E*).

Like other apicomplexan zoites (10, 23, 24), *P. knowlesi* merozoites appear to undergo corkscrew-like rotation (*SI Appendix,* Movie S5), with a correlation between the number of turns and forward translocation, indicating a link between the two motions (Fig. 2*C* and *D*). On average, for each body length the merozoite moved forward, it rotated 0.8 times – equivalent to a tangential velocity of 1 μm/second (n = 10 merozoites). This is consistent with a linear motor running at a 42-degree angle down the longitudinal axis of the merozoite. Nine out of ten merozoites rotated counterclockwise, demonstrating the same chirality seen for *Plasmodium* ookinetes (25). Rotation could not be discerned for *P. falciparum* merozoites, likely due to the round morphology and small size.

For both *Plasmodium* species, gliding and invasion proceeded with the wider end of the merozoite leading, rather than the narrower pointed end (Fig. 2*D*). The narrower, pointed end has been widely suggested to contain the apical complex of the parasite, and indeed is consistent with early images of invading parasites by transmission electron microscopy (26). To test whether the apical complex is instead located at the wider end of the parasite, we examined *P. knowlesi* parasites expressing mNeonGreen-tagged apical membrane antigen 1 (AMA1-mNG) using live microscopy. Movie S6 clearly shows that the apical end is located at the wider end of the zoite (Fig. 2*E*), and that host cell entry proceeds in the same orientation as surface gliding, as observed previously for *B. bovis* merozoites (24). Imaging of the AMA1-mNG parasites also shows, for the first time using live microscopy to image *Plasmodium* invasion, the formation of a ring structure of the tight junction as the parasite invades the host erythrocyte (Fig. 2*E* and *SI Appendix,* Movie S6). A small protrusion likely corresponding to the apical complex is visible slightly offset from the apex of the wider front-end (Fig. 2*F*, left hand image). It is the accentuation of this during the constriction of invasion depicted within classic electron microscopy images which has likely led to the general assumption that merozoites uniformly narrow towards the apical end (Fig. 2*F*). Whilst this is most clearly seen in the elongated forms of the *P. knowlesi* merozoites, it is also demonstrated in videos of gliding in *P. falciparum* (*SI Appendix,* Movie S2).

Merozoites also exhibited helical motility during host cell entry and after internalization within the host cell, as has been described for invading *T. gondii* tachyzoites (27). This event can be seen when observing apically localized AMA1-mNG, which rotates around the plane of the moving junction in an anti-clockwise manner during entry and then again rapidly for several seconds post internalization

192 (*SI Appendix,* Movie S6). Thus, like other zoites, *Plasmodium* merozoites appear to
193 enter host cells using a corkscrew-like mechanism. Post entry spinning, as recently
194 visualized with 4D lattice light sheet microscopy for invading *P. falciparum* parasites
195 (28) may, in turn, facilitate twisting and separation of the newly formed
196 parasitophorous vacuole from the erythrocyte plasma membrane.
197
198
199 **Gliding motility is powered by an actomyosin motor and glideosome complex**
200 To determine the characteristics of the *P. falciparum* merozoite glideosome we
201 evaluated the effect of chemical compounds and parasite genetic modifications on
202 merozoite gliding motility. In comparison to *P. knowlesi*, *P. falciparum* merozoites
203 appear to be more vulnerable to light (29) and often lose their ability to invade
204 erythrocytes when exposed to even small amounts of light, complicating the
205 observation of their gliding movement by light microscopy. In our hands, schizonts
206 exposed to light over several minutes often showed very few motile merozoites (*SI*
207 *Appendix,* Movie S7). On average, only roughly 6% (2/32) of schizonts released 70%
208 or more gliding merozoites, where a 'glide' was defined as forward movement for at
209 least 5 continuous seconds (*SI Appendix,* Fig. S3*A* and Movie S2). Thus, to overcome
210 the light sensitivity of *P. falciparum* merozoites we developed an assay in which
211 schizonts were seeded and incubated in the dark on coverslips for 1 hour 37°C until
212 the completion of merozoite egress. Motility could then be quantified by measuring the
213 distance between a DAPI-stained merozoite nucleus and the hemozoin in the residual
214 body (Fig. 3*A*). In comparing with DMSO-treated merozoites (100%), 0.1, 1, and 10
215 μM cytochalasin (IC_{50} = 0.085 μM) D treatment significantly reduced the merozoite-
216 hemozoin distance (77.9%; IQR = 25.1%, 52.6%; IQR = 28.2%, and 50.9%; IQR =

217 16.5%, respectively). Treatment with jasplakinolide, an actin filament stabilizer
218 reported to increase the speed of *T. gondii* tachyzoites, did not significantly increase
219 the distance travelled by *P. falciparum* merozoites (Fig. 3*B* and *SI Appendix,* S3).
220 We next examined the effects of the conditional deletion of two essential
221 glideosome components, ACT1 (16) and GAP45 (17). Transgenic lines were able to
222 egress after both the control DMSO treatment and upon rapamycin induced gene
223 excision, but the merozoite–hemozoin distance was significantly reduced after
224 deletion of either ACT1 or GAP45 (Fig. 3*C*). When AMA1, a microneme protein
225 important for erythrocyte invasion but unlikely to be involved in merozoite motility (30,
226 31) was conditionally deleted, parasites were able to efficiently egress and move
227 across the substrate (*SI Appendix,* Fig. S4). These results confirm the requirement of
228 the glideosome for *Plasmodium* merozoite gliding motility.
229
230 **Gliding motility is regulated by a complex signaling pathway**
231 Microneme discharge plays an essential role in the egress, gliding motility, and cell
232 invasion of apicomplexan parasites and is regulated by a set of intracellular signaling
233 enzymes, including calcium-dependent protein kinases (32, 33), phosphoinositide-
234 phospholipase C (PI-PLC) (34), and diacylglycerol (DAG) kinase (35). We evaluated
235 whether these enzymes are also involved in the gliding motility of *P. falciparum*
236 merozoites. Although the calcium ionophore A23187 (up to 100 μM) did not show a
237 significant effect, the calcium chelator BAPTA-AM (10 μM) significantly reduced
238 merozoite–hemozoin distance ($p < 0.0001$; Fig. 3*D* and *SI Appendix,* S3*B*). The PLC
239 inhibitor U73122 (1 μM), but not the inactive analog U73343 (up to 10 μM), significantly
240 reduced merozoite–hemozoin distance ($p < 0.0001$). The DAG kinase inhibitor
241 R59022 (3 μM), which inhibits the conversion of DAG to phosphatidic acid (PA) also

242 significantly reduced movement ($p < 0.001$); while the merozoite–hemozoin distance
243 was not changed with propranolol, an inhibitor of phosphatidate phosphohydrolase
244 (the converter of PA to DAG). Collectively, these results are consistent with reports on
245 *Toxoplasma* tachyzoites (35) and indicate that complex signaling pathways are
246 involved in gliding motility of *P. falciparum* merozoites (Fig. 3*E*).
247

248 **Gliding motility facilitates erythrocyte-specific interactions and underpins**
249 **important precursor steps to invasion**

250 Having established the characteristics of merozoite motility and its regulation, we next
251 sought to understand whether gliding may play a role during erythrocyte invasion in
252 addition to host cell entry, and whether this function might also facilitate movement of
253 merozoites across alternative cellular surfaces. Prior to host cell entry, merozoite-
254 erythrocyte interactions cause the erythrocyte membrane to deform, often resulting in
255 the entire erythrocyte "wrapping" around the merozoite (7). Several studies have
256 highlighted the importance of deformation as a mechanism merozoites use to commit
257 to host cell entry and have demonstrated that the merozoite's molecular motor is
258 required for deformation (16, 17, 36). However, the precise mechanism behind this
259 phenomenon has not been elucidated. In good agreement with previous work, we
260 found that not only were rapamycin-treated ACT1- or GAP45-deleted *P. falciparum*
261 parasites unable to glide, but they were also unable to deform erythrocytes (Fig. 4*A*
262 and *B*). Thus, we reasoned that gliding motility itself may be required for erythrocyte
263 deformation.

264 Due to our finding that the majority of *P. knowlesi* merozoites do not disperse
265 from each other when gliding is inhibited with cytochalasin D, we could not easily
266 measure the impact of gliding inhibition on erythrocyte deformation for this species.

267 However, the larger size and more pronounced morphology of *P. knowlesi* merozoites
268 did allow us to visualize the deformation process of wild type merozoites more clearly.
269 Deformation did not appear to simply be the result of the merozoite attempting to be
270 internalized in the erythrocyte, as previously hypothesized (6). Rather, deformation
271 was marked by a wrapping of the erythrocyte membrane down the length of a forward
272 moving merozoite, horizontally aligned with the erythrocyte surface. Notably,
273 deformation began as a merozoite initiated gliding across a host cell surface, with
274 waves of deformation often travelling from the zoite's apical prominence to the basal
275 end (Fig. 4*C* and *SI Appendix,* Movie S8). These sum results indicate that not only
276 does gliding motility coincide with erythrocyte deformation, but also that the two
277 processes are mechanically linked.

278 Recently, both sexual and asexual stages of multiple *Plasmodium* species have
279 been identified within bone marrow compartments (37-39). This raised the question of
280 whether merozoites may be able to glide on endothelial surfaces and/or within
281 extravascular compartments, such as the bone marrow. Yet how do *Plasmodium*
282 parasites exit the bloodstream and enter tissues? One possibility is that parasitized
283 reticulocytes may be returning to extravascular environments via extravasation.
284 However, another mechanism could be that free merozoites are capable of gliding
285 across endothelial barriers and into tissues (40, 41). To test the latter theory, we
286 examined *P. knowlesi* parasites egressing on either primary human umbilical vein
287 (HUVEC) or dermal endothelial cell lines. Rather surprisingly, we found that *P.*
288 *knowlesi* merozoites were unable to adhere to or demonstrate motility across either
289 cell line (Fig. 4*D* and *SI Appendix,* Movie S9). Similar results were obtained when
290 endothelial cells were pre-treated with tumor necrosis factor (TNF), an inflammatory
291 cytokine known to increase the expression of endothelial adhesive surface ligands (Fig.

292 4*D*) (42). Thus, whilst these results do not rule out the possibility of gliding within tissue
293 compartments, they do suggest that gliding is unlikely to support extravasation of free
294 merozoites and that merozoite motility may be specific to erythrocyte lineages and
295 highly adherent artificial surfaces, in strong contrast to other zoites which can glide
296 successfully on a broad array of substrates.

297 Despite the finding that merozoites are unlikely to use gliding to move across
298 endothelial barriers, we did observe that freshly egressed *P. knowlesi* merozoites often
299 glide across several different human erythrocytes prior to invading their host cell of
300 choice (*SI Appendix,* Movie S10). Thus, we reasoned that in addition to facilitating
301 erythrocyte deformation, gliding may enable merozoites to contact multiple
302 erythrocytes, in the event they are unable to invade the first host cell they encounter.
303 Studies have shown that most invading *P. falciparum* merozoites (~85%) will invade
304 the first cell they contact (36); however, we found that only 26% (10/38 invasions) of
305 invading *P. knowlesi* merozoites invaded the first human erythrocyte they contacted,
306 and a significant proportion of merozoites (~32%, or 12/38 events) contacted 4 to 7
307 unique cells prior to committing to invasion (Fig. 4*E*). We hypothesized that this stark
308 difference between species may be because, unlike *P. falciparum*, the natural host
309 cells of *P. knowlesi* are not human, but rather macaque erythrocytes (22). Thus *P.*
310 *knowlesi* merozoites may need to contact more human erythrocytes overall, to
311 encounter an erythrocyte amenable to invasion. In support of this theory, we found
312 that on average, *P. knowlesi* merozoites contacted significantly fewer macaque
313 erythrocytes prior to invasion (Fig. 4*E*), with the vast majority of merozoites (85%)
314 invading either the first or second macaque cell they contacted. Therefore, these
315 results indicate that gliding could contribute to the zoonotic potential of *P. knowlesi*

316 and may explain how merozoites of multiple species navigate strict erythrocyte tropism

317 requirements to proliferate under sub-optimal conditions.

Discussion

In this work, we show for the first time that *Plasmodium* merozoites undergo gliding motility and demonstrate productive movement across coverslip and erythrocyte surfaces for two human infective species: *P. falciparum* and *P. knowlesi*. Motility was more evident for *P. knowlesi* merozoites, which in our hands were found to glide on average nearly twice as fast and for 7 times longer than *P. falciparum* merozoites.

Since the first, and landmark video microscopy of *P. knowlesi* in 1975 (6), no further imaging studies have been published for this species. This, in combination with the frequent use of glass slides to image parasites, rather than the polymer coverslips that were used for this study, may explain in part why motility was not observed in *P. falciparum* invasion studies. However, our retrospective analysis of published data shows several subtle examples of *P. falciparum* merozoites completing short glides across human erythrocytes, such as videos from Treek et al., 2009 (Video S4, from 25-70 seconds) (30) and Weiss et al., 2015 (Video S13, from 0-26 seconds) (36).

Our work, in good agreement with previous studies (16, 17, 36), shows that without motor function merozoites cannot glide across cellular surfaces or deform host erythrocytes. Thus, gliding motility is likely an important requirement for deformation. While deformation itself is not an essential invasion step for *P. falciparum*, strong deformation has been positively correlated with invasion success and is predicted to increase the efficiency of the host cell selection process (36). Therefore, by extension, gliding is also likely to facilitate these key steps, increasing the likelihood of each merozoite-erythrocyte contact progressing into invasion.

Having clearly demonstrated gliding motility in static in vitro cultures, it will be important to determine how this mechanism translates to flow conditions found *in vivo*. Whilst the feasibility of cell-cell transfer is yet to be tested under flow conditions, live

343 *in vivo* imaging of erythrocytes flowing through human capillaries shows that
344 erythrocytes are frequently attached to each other for prolonged periods of time,
345 travelling together at roughly the same speed (43). Therefore, in theory, flowing
346 erythrocyte "bridges" may facilitate merozoite movement from cell to cell *in vivo*.

347 Erythrocytes are known to be highly heterogeneous, in terms of maturity,
348 surface receptor density, and membrane tension properties (44). As such, motility
349 could also enable merozoites to contact a wider range of erythrocytes in the
350 bloodstream, whereby the parasite moves around the surface of an individual
351 erythrocyte, or across the surfaces of multiple erythrocytes until it is able to engage
352 with a critical threshold of invasion receptors or select a cell with favorable
353 characteristics for invasion. Our work has shown that only 26% of *P. knowlesi*
354 merozoites invade the first human erythrocyte they contact, with the vast majority
355 instead contacting multiple cells before committing to invasion. Notably, *P. knowlesi*
356 exhibits a preference (not restriction) for younger erythrocytes when cultured with
357 human erythrocytes (45, 46). Thus, gliding may be a critical mechanism *P. knowlesi*
358 merozoites use to successfully proliferate in human hosts.

359 A greater proportion of *P. knowlesi* merozoites will invade the first macaque
360 erythrocyte they contact (~ 46%), in line with their preference for their natural host cells
361 (macaque erythrocytes) over human cells (45). In contrast, most *P. falciparum*
362 merozoites (~86% of 3D7 parasites) invade the first human erythrocyte they encounter
363 (36), therefore, the ability to contact multiple cells is likely to be less important for *P.*
364 *falciparum*, and instead gliding may simply enhance erythrocyte receptor interactions
365 on any given cell.

366 One reason for these distinct strategies could be that each species possesses
367 highly divergent sets of RBL/Rh and DBP/EBA ligands - two critical families of invasion

368 ligands which are key determinants of host cell tropism and are predicted to facilitate
369 host cell selection (36, 47). Differing expression profiles, along with differing levels of
370 receptor abundance and availability within erythrocyte populations, likely impact how
371 efficiently merozoites can "commit" to invasion, and thus their need to contact different
372 cells. At one extreme, for *P. vivax* a single DBP ligand and selection of RBL ligands
373 restricts this species to growth in Duffy positive human reticulocytes (48, 49). Since
374 reticulocytes make up less than 2% of red blood cells circulating within the
375 bloodstream (50), gliding motility may enable *P. vivax* merozoites to roam and
376 eventually encounter reticulocytes.

377 It is also plausible that motility supports translocation and invasion within tissues
378 such as the bone marrow, which is known to be a significant parasite reservoir for *P.*
379 *vivax* (39). Parasites may accumulate within the bone marrow via extravasation: the
380 crossing of either infected reticulocytes or free merozoites into the bone marrow
381 parenchyma via a layer of endothelial cells lining the sinusoidal capillaries (40, 41).
382 However, we did not observe merozoite motility across endothelial surfaces; an
383 outcome which suggests that gliding may not support extravasation of free merozoites.
384 Notably, though, *P. vivax* merozoites have been shown to exhibit a preference for the
385 CD71-positive youngest reticulocytes found predominantly within the bone marrow
386 prior to further maturation and intravasation (40). This suggests that at least some
387 invasions may take place within the bone marrow parenchyma itself, contributing to
388 the overall parasite burden within this tissue. Thus, gliding may enable merozoites that
389 have egressed within the bone marrow to specifically target these young reticulocytes
390 in this richly diverse cellular environment.

391 Our work also enabled us to reverse the dogma perception of the morphology
392 of merozoites, with clear evidence from both gliding and fluorescently tagged parasites

393 demonstrating that the apical complex resides in a small protrusion in the wider end
394 of the zoite, rather than the pointed end of a teardrop shape as it is often depicted (51).
395 *Plasmodium* ookinetes also lead with their wider end (18), and thus it must be
396 reevaluated how we interpret images of invasion and understand the biophysical
397 processes involved (51).

398 Our displacement assay also enabled us to test the impact of various inhibitors
399 of calcium signaling pathways, previously shown to be important for microneme
400 secretion (34) and invasion (34, 36) for *Plasmodium* parasites. Our results are in good
401 agreement with data from these studies; however, ascribing function based on inhibitor
402 data alone can be challenging. For instance, although our work shows that the inhibitor
403 U73122, but not its inactive analog, U73343, inhibits signaling pathways also predicted
404 to be required for motility; in other systems, the effects of both compounds have been
405 shown to be identical, suggesting off-target activity (52). Therefore, future work should
406 include targeted genetic approaches such as conditional knockout studies ablating
407 signaling enzymes – something which is now readily achievable for *Plasmodium* blood
408 stages in both *P. knowlesi* and *P. falciparum* (53).

409 One of the outstanding questions is which parasite proteins are required for
410 bridging the motor to host cell ligands to enable gliding motility. Apicomplexan zoites
411 utilize type I transmembrane proteins belonging to the TRAP family to adhere to
412 environmental substrates for gliding. Two such proteins, merozoite thrombospondin-
413 related anonymous protein (MTRAP) and thrombospondin-related apical membrane
414 protein (TRAMP or PTRAMP), are expressed at the merozoite stage (54). MTRAP is
415 dispensable for *P. falciparum* and *P. berghei* merozoites (55); however, multiple
416 studies indicate that TRAMP is essential for the blood stage parasite (56, 57), making
417 it a prime candidate for future work to identify a merozoite gliding adhesin. Our gliding

418 assays can greatly facilitate the identification of such proteins and their roles during
419 invasion.

420 In conclusion, *Plasmodium* merozoites have the capacity for gliding motility,
421 powered by a conserved actomyosin motor and glideosome complex, and controlled
422 by a complex signaling cascade. The distinct gliding profiles of two different human
423 infective species suggest divergent invasion strategies which provide new
424 mechanisms to address questions of host selectivity and tissue reservoirs of the
425 erythrocytic stages.

426 **Materials and Methods**

427 **Parasite culture and transfection**

428 *P. falciparum* Dd2 parasites were maintained with O^+ human erythrocytes in
429 RPMI1640 medium (Invitrogen, CA, USA) supplemented with 25 mM HEPES (Sigma,
430 St. Louis, USA), 0.225% sodium bicarbonate (Invitrogen), 0.1 mM hypoxanthine
431 (Sigma), 25 µg/mL gentamicin (Invitrogen), 0.5% AlbuMax I (Invitrogen), essentially
432 as described (59). The ACT1 (16), GAP45:loxP (17), and AMA1:loxP *P. falciparum*
433 lines (60) were cultured with A^+ human erythrocytes. WR99210 and G418 were used
434 to generate ACT1 and AMA1:loxP parasite lines, respectively. *P. yoelii* 17XNL
435 parasites were intravenously inoculated into ICR mice (SLC Inc., Shizuoka, Japan).
436 Animal experiments were approved by the Animal Care and Use Committee of
437 Nagasaki University (Permit number: 1403031120-5). The *T. gondii* RH strain was
438 cultured in a confluent monolayer of human foreskin fibroblasts (HFFs) maintained in
439 Dulbecco's Modified Eagle Medium (DMEM), GlutaMAX supplemented with 10% fetal
440 bovine serum, at 37°C and 5% CO_2. The *B. bovis* Texas strain was maintained in
441 purified bovine erythrocytes with GIT medium (WAKO, Osaka, Japan) at 37°C with a
442 microaerophilic stationary-phase culture system. A1-H.1 *P. knowlesi* parasites were
443 maintained in human erythrocytes (UK National Blood Transfusion Service) with
444 custom made RPMI-1640 medium, supplemented with 10% Horse Serum (v/v) and 2
445 mM L-glutamine according to previously described methods (22). Mature schizonts
446 were purified by gradient centrifugation on a 55% Nycodenz layer (Progen,
447 Heidelberg, Germany), as described (22). Tightly synchronized schizonts were
448 transfected using the Amaxa 4-D electroporator and P3 Primary Cell 4D Nucleofector
449 X Kit L (Lonza) according to the protocol described by Moon *et al*. (22).

450

451 **Generation of *P. knowlesi* parasites with mNeonGreen-tagged AMA1**

452 *P. knowlesi* parasites with mNeonGreen-tagged AMA1 were generated by insertion of
453 an mNeonGreen sequence immediately before the *AMA1* stop codon (*SI Appendix,*
454 Fig. S2*A*) using the CRISPR-Cas9 system described by Mohring *et al.* (61) (sgRNA
455 sequence: GAGAAGCCTTACTACTGAGT). Donor DNA was synthesized by
456 overlapping PCR, as previously described for PkAMA1-HA tagged parasites (61) and
457 included the mNeonGreen sequence flanked by 500 bp sequences homologous to the
458 C-terminal (HR1) and 3'UTR (HR2) regions of the AMA1 locus (*SI Appendix,* Fig. S2*A*).
459 Primers for PCR are listed in Table S1. In brief, HR1 and HR2 were both PCR-
460 amplified from *P. knowlesi* A1-H.1 gDNA (with primers P6/P7 and P8/P9, respectively),
461 while the mNeonGreen sequence was amplified from plasmid Pk_mNeonGreen with
462 primers P10/P11. All three fragments were subsequently assembled together in two
463 successive steps: firstly by fusing fragments HR1 and mNeonGreen (primers
464 P12/P13), and secondly by fusing fragments HR1/mNeonGreen and HR2 (primers
465 P12/P15) to create the final product, HR1/mNeonGreen/HR2. Post transfection,
466 integration of donor DNA was confirmed by diagnostic PCR, using primers P1 and P3
467 (*SI Appendix,* Fig. S2*B*). Expression of the AMA1-mNeonGreen fusion protein was
468 also confirmed by indirect immunofluorescence assay (*SI Appendix,* Fig. S2*C*). Air-
469 dried smears of late stage schizonts were fixed in 4% paraformaldehyde for half an
470 hour and permeabilised with PBS containing 0.1% Triton-X100 for 10 minutes. Slides
471 were subsequently blocked overnight in PBS containing 3% BSA before labelling with
472 anti-mNeonGreen mouse monoclonal antibody (32F6; 1:300; Chromotek, Germany)
473 followed by Alexa Fluor 488 goat anti-mouse antibody (1:1000, Invitrogen). Nuclei

474 were stained with DAPI (Invitrogen) and mounted with ProLong Gold antifade reagent
475 (Invitrogen). Images were collected using an inverted microscope (Ti-E; Nikon, Japan)
476 with a 60x oil objective lens (N.A. 1.4).

477

478 **Inducible gene-knockout *P. falciparum* parasites**

479 The *GAP45*, *Act1*, and *AMA1* genes were excised by rapamycin treatment from
480 GAP45:loxP, ACT1, and AMA1:loxP *P. falciparum* parasites, respectively (62). Briefly,
481 ring stage parasites synchronized by 5% sorbitol method were treated with 100 nM
482 rapamycin (Sigma) or 0.1% DMSO for 12 hours. Schizonts were purified with a CS
483 magnet separation column (MACS, Miltenyi Biotech, Germany) and used for gliding or
484 erythrocyte invasion assays.

485

486 **Endothelial cell culture and stimulation**

487 Commercially available primary human dermal microvascular endothelial cells
488 (HDMVECs, ScienCell, Carlsbad, CA) and umbilical vein endothelial cells (HUVECs,
489 ScienCell) were cultured at 37ºC with 5% CO_2 on fibronectin-coated 6-channel μ-
490 Slides (ibidi, Germany) and grown to confluence in DME/F12 medium (Thermo Fisher,
491 Waltham, MA), pH 7.4, supplemented with 10% fetal bovine serum (ScienCell), 30
492 μg/mL endothelial cell growth supplement (Sigma), and 10 μg/mL gentamycin
493 (Thermo Fisher). Cells were rinsed with sterile PBS (Sigma) and fresh medium was
494 added 18 hours prior to the gliding assays, with or without 10 pg/mL recombinant
495 human tumor necrosis factor alpha (TNFα, PeproTech, Rocky Hill, NJ). Primary
496 HDMVECs and HUVECs were used between passage 2 and 3 for all experiments.

497

498 **Time lapse imaging for the gliding motility**

499 Time lapse imaging assays for *P. falciparum* merozoites were performed at 37ºC using
500 an inverted microscope (Ti-E; Nikon) with a 60x oil objective lens (N.A. 1.4 or 1.47). *P.*
501 *falciparum* synchronized-schizonts in incomplete medium without AlbuMAX I were
502 transferred to the ibiTreat μ-Slide $I^{0.4}$ Luer channel slide (ibidi) and incubated for 10
503 minutes at 37ºC to allow the parasite-infected erythrocytes to attach to the bottom.
504 Incomplete medium was removed and replaced with complete RPMI medium
505 prewarmed to 37ºC, then parasites were observed by microscopy. Likewise,
506 synchronized *P. knowlesi* schizonts were transferred using the same technique to
507 either ibiTreat, poly-L-lysine-coated, uncoated, or glass μ-Slide $I^{0.4/0.5}$ Luer channel
508 slides (ibidi) in incomplete RPMI medium and incubated at 37ºC for 10 minutes to allow
509 cell attachment. Subsequently, incomplete medium was replaced with complete RPMI
510 medium with 10% horse serum, as per normal culturing conditions. For the actin
511 inhibitor treatments, *P. knowlesi* schizonts were allowed to attach to coverslips while
512 suspended in incomplete RPMI medium, which was then replaced with complete RPMI
513 medium additionally containing 0.1 μM cytochalasin D (Sigma) or 0.1% DMSO (Sigma).
514 For experiments visualizing *P. knowlesi* egress, schizonts were first incubated with 10
515 μg/mL wheatgerm agglutinin for 10 minutes at 37ºC. Schizonts were subsequently
516 washed 2 times in RPMI medium before loading into channel slides for drug treatment
517 as described above. For *P. knowlesi* invasion assays, purified schizonts were added
518 to fresh human (UK National Blood Transfusion Service) or cynomolgus macaque
519 (Silabe) erythrocytes to make a 5-10% parasitaemia and 2.5% haematocrit culture.
520 The haematocrit was subsequently adjusted to 0.25%, and 150 μL culture was loaded
521 into a PLL-coated μ-Slide VI 0.4 (ibidi). *P. yoelii* sporozoites were isolated in RPMI

522 medium from parasite infected mosquito midguts as described (63), then isolated
523 sporozoites were transferred to an ibiTreat μ-Slide $I^{0.4}$ Luer channel slide. *T. gondii*
524 tachyzoites growing in HFFs were collected by scraping after the culture medium was
525 replaced with ENDO buffer (64). Intracellular parasites were isolated from HFFs by
526 lysing host cells via passaging 20 times through a syringe and tachyzoites were
527 transferred to an ibiTreat μ-Slide $I^{0.4}$ Luer channel slide and incubated for 15 minutes
528 at 37ºC. The slide was placed on the microscope stage, and the medium was replaced
529 with DMEM before observation. *B. bovis* parasites were isolated in RPMI medium then
530 transferred to the ibiTreat μ-Slide $I^{0.4}$ Luer channel slide. All parasites were observed
531 by differential interference contrast or bright field at 1.5V/100W of halogen lamp or
532 LED light (pT-100; CoolLED, UK) to minimize cell damage. Time-lapse images were
533 captured at 1–100 frames per second using a digital camera (ORCA-R2 or ORCA-
534 Flash4.0; Hamamatsu photonics, Shizuoka, Japan) and imaged using the NIS-
535 Element Advanced Research imaging software (Nikon). The speed of individual
536 merozoites was calculated by tracking actively moving merozoites either manually,
537 using distance measurement tools, or by the tracking module within the NIS-Element
538 software (Nikon). The tangential speed of *P. knowlesi* merozoites was determined by
539 calculating the number of rotations/minute and multiplying this value by the average
540 circumference of a merozoite. The angle of the motor was subsequently calculated
541 using the formula Tan(x) = R/L, where x = the angle of the motor, R = the average
542 distance each merozoite rotated/per body length travelled forward, and L = the body
543 length of the merozoite.

544

545 ***P. falciparum* merozoite gliding assay**

546 *P. falciparum* schizonts were purified with a CS magnet separation column, then
547 adjusted to 1 x 10^5 cell/mL with incomplete RPMI medium and loaded onto an ibiTreat
548 μ-Slide $VI^{0.4}$ channel slide (ibidi). The channel slides were incubated for 10 minutes at
549 17°C to allow schizont attachment to the bottom followed by replacing the medium
550 with complete RPMI medium containing chemical compounds or DMSO control. Slides
551 were incubated at 17°C for 1 hour then the temperature was increased to 37°C for 1
552 hour to allow parasite egress. Parasites were fixed with 1% paraformaldehyde fixation
553 solution, which was then replaced with PBS containing 3% BSA (Sigma) and 100
554 ng/mL DAPI. For the indirect immunofluorescence assay, parasites were fixed in 4%
555 paraformaldehyde containing 0.0075% glutaraldehyde (Nacalai Tesque, Japan) and
556 permeabilized with PBS containing 0.1% Triton-X100 (Calbiochem, CA, USA), then
557 blocked with PBS containing 3% BSA. Next, samples were immunostained with mouse
558 anti-*P. falciparum* ACT1 (final dilution 1:500; a kind gift from Jake Baum) or rat anti-
559 HA (1:1000; Roche, Basel, Switzerland) for HA-tagged GAP45 and AMA1. This was
560 followed by 3 × washes with PBS then incubation with Alexa Fluor 488 goat anti-mouse
561 or Alexa Fluor 594 goat anti-rat antibodies (1:1000; Invitrogen) in PBS containing 3%
562 BSA with DAPI. Stained parasites were mounted with Prolong Gold antifade reagent.
563 Microscopy images (Ti-E, Nikon) of egressed merozoites were cropped to 47 x 47 μm^2
564 to measure the distance of merozoite nuclei (stained with DAPI) from hemozoin in the
565 residual body (malaria pigment, with bright field image) using NIS-Elements software
566 (Nikon). Statistical analysis was performed by the Kruskal-Wallis test followed by
567 Dunn's multiple comparison test using PRISM 6 software (GraphPad Software, Inc.,
568 CA, USA).

569

570 **Chemical Compounds**

571 Complete RPMI medium was supplemented with cytochalasin D, jasplakinolide
572 (Sigma), 1,2-Bis(2-aminophenoxy)ethane-N,N,N',N'-tetraacetic acid
573 tetraacetoxymethyl ester (BAPTA-AM, Invitrogen), calcium Ionophore A23187
574 (Sigma), U73122 (Calbiochem), U73343 (Calbiochem), R59022 (Tocris bioscience,
575 UK), propranolol (Sigma), or DMSO. Compound concentrations were as described (33,
576 34). IC_{50} values for *P. falciparum* were determined using a protocol available at
577 WorldWide Antimalarial Resistance Network (WWARN-
578 http://www.wwarn.org/sites/default/files/INV08_PFalciparumDrugSensitivity.pdf).

579

References

1. D. G. Russell, R. E. Sinden, The role of the cytoskeleton in the motility of coccidian sporozoites. *J. Cell. Sci.* **50**: 345-59 (1981).
2. J. M. Dobrowolski, L. D. Sibley, Toxoplasma invasion of mammalian cells is powered by the actin cytoskeleton of the parasite. *Cell* **84**, 933–939 (1996).
3. B. Danilewsky, *La Parasitologie Comparée du Sang.* Kharkoff (1889).
4. B. Grassi, *Studi di uno zoologo sulla malaria.* R. Accademia dei Lincei (1900).
5. M. YOELI, Movement of the Sporozoites of *Plasmodium berghei* (Vincke et Lips, 1948). *Nat. 1964 2014926* **201**, 1344–1345 (1964).
6. J. A. Dvorak, L. H. Miller, W. C. Whitehouse, T. Shiroishi, Invasion of erythrocytes by malaria merozoites. *Science* **187**, 748–750 (1975).
7. P. R. Gilson, B. S. Crabb, Morphology and kinetics of the three distinct phases of red blood cell invasion by *Plasmodium falciparum* merozoites. *Int. J. Parasitol.* **39**, 91–6 (2009).
8. K. Yahata, M. Treeck, R. Culleton, T. W. Gilberger, O. Kaneko, Time-lapse imaging of red blood cell invasion by the rodent malaria parasite *Plasmodium yoelii*. *PLOS ONE* **7,** e50780 (2012).
9. I. Tardieux, J. Baum, Reassessing the mechanics of parasite motility and host-cell invasion. *J. Cell. Biol.* **214**:507–515 (2016)
10. S. Hakansson, H. Morisaki, J. Heuser, L. D. Sibley, Time-lapse video microscopy of gliding motility in *Toxoplasma gondii* reveals a novel, biphasic mechanism of cell locomotion. *Mol. Biol. Cell.* **10**:3539–47 (1999).
11. K. Frenal, J. F. Dubremetz, M. Lebrun, D. Soldati-Favre, Gliding motility powers invasion and egress in Apicomplexa. *Nat. Rev. Microbiol.* **15**, 645–660 (2017).

12. G. Pavlou *et al. Toxoplasma* parasite twisting motion mechanically induces host cell membrane fission to complete invasion within a protective vacuole. *Cell Host Microbe* **24**, 81-96.e5 (2018).

13. C. Opitz, D. Sordati, “The glideosome”: a dynamic complex powering gliding motion and host cell invasion by Toxoplasma gondii. *Mol. Microbiol.* **45**, 597–604 (2002).

14. J. Baum *et al.*, A conserved molecular motor drives cell invasion and gliding motility across malaria life cycle stages and other apicomplexan parasites. *J. Biol. Chem.* **281**, 5197–5208 (2006).

15. J. Robert-Paganin, *et al.*, Plasmodium myosin A drives parasite invasion by an atypical force generating mechanism. *Nat. Commun. 2019 101* **10**, 1–12 (2019).

16. S. Das, L. Lemgruber, C. L. Tay, J. Baum, M. Meissner, Multiple essential functions of *Plasmodium falciparum* actin-1 during malaria blood-stage development. *BMC Biol.* **15**: 70 (2017).

17. A. J. Perrin *et al.* The actinomyosin motor drives malaria parasite red blood cell invasion but not egress. *mBio* **9**, e00905-18 (2018).

18. R. W. Moon, *et al*., A cyclic GMP signalling module that regulates gliding motility in a malaria parasite. *PLoS Pathog.* **9**, e1000599 (2009).

19. M. J. Boyle *et al.* Isolation of viable *Plasmodium falciparum* merozoites to define erythrocyte invasion events and advance vaccine and drug development. *Proc. Natl Acad. Sci. USA* **107**, 14378–14383 (2010).

20. E. D. Dennis, G. H. Mitchell, G. A. Butcher, S. Cohen, In vitro isolation of *Plasmodium knowlesi* merozoites using polycarbonate sieves. *Parasitology* **71**, 475–481 (1975).

21. O. Lyth *et al.* Cellular dissection of malaria parasite invasion of human erythrocytes using viable *Plasmodium knowlesi* merozoites. *Sci. Rep.* **8**, 10165 (2018)

22. R. W. Moon *et al.* Adaptation of the genetically tractable malaria pathogen *Plasmodium knowlesi* to continuous culture in human erythrocytes. *Proc. Natl Acad. Sci. USA* **110**, 531–536 (2013).

23. M. Kudryashev *et al.* Structural basis for chirality and directional motility of *Plasmodium* sporozoites. *Cell Microbiol*. **14**:1757–68 (2012).

24. M. Asada *et al.* Gliding motility of *Babesia bovis* merozoites visualized by time-lapse video microscopy. *PLoS One* **7**, e35227 (2012).

25. A. Kan *et al.* Quantitative analysis of *Plasmodium* ookinete motion in three dimensions suggests a critical role for cell shape in the biomechanics of malaria parasite gliding motility. *Cell. Microbiol*. ***5***, 734–750 (2014).

26. L. H. Miller, M. Aikawa, J. G. Johnson, T. Shiroishi, Interaction between cytochalasin B-treated malarial parasites and erythrocytes: Attachment and junction formation. *J. Exp. Med*. **149**, 172-184 (1979).

27. G. Pavlou *et al., Toxoplasma* parasite twisting motion mechanically induces host cell membrane fission to complete invasion within a protective vacuole. *Cell Host Microbe* **24**, 81-96.e5 (2018).

28. N. D. Geoghegan, *et al.*, 4D analysis of malaria parasite invasion offers insights into erythrocyte membrane remodeling and parasitophorous vacuole formation. *Nat. Commun.* **12**, 3620 (2021).

29. F. Wissing, C. P. Sanchez, P. Rohrbach, S. Ricken, M. Lanzer, Illumination of the malaria parasite *Plasmodium falciparum* alters intracellular pH. Implications for live cell imaging. *J. Biol. Chem.* **277**, 37747–37755 (2002).

30. M. Treeck *et al.* Functional analysis of the leading malaria vaccine candidate AMA-1 reveals an essential role for the cytoplasmic domain in the invasion process. *PLOS Pathog*. **5**: e1000322 (2009).

31. A. S. Yang *et al.* Molecular mechanisms of host cell traversal by malaria sporozoites. *Int. J. Parasitol.* **47**, 129-136 (2017).

32. O. Billker, S. Lourido, L. D. Sibley, Calcium-dependent signaling and kinases in apicomplexan parasites. *Cell Host Microbe* **5**, 612–622 (2009).

33. D. A. Baker, Cyclic nucleotide signalling in malaria parasites. *Open Biol.* **12**, (2017).

34. S. Singh, M. M. Alam, I. Pal-Bhowmick, J. A. Brzostowski, C. E. Chitnis, Distinct external signals trigger sequential release of apical organelles during erythrocyte invasion by malaria parasites. *PLOS Pathog*. **6**, e1000746 (2010).

35. H. E. Bullen *et al.* Phosphatidic acid-mediated signalling regulates microneme secretion in *Toxoplasma*. *Cell Host Microbe* **19**, 349–360 (2016).

36. G. E. Weiss, *et al.,* Revealing the sequence and resulting cellular morphology of receptor-ligand interactions during *Plasmodium falciparum* invasion of erythrocytes. *PLoS Pathog*. 11, 1004670 (2015).

37. R. Joice, *et al., Plasmodium falciparum* transmission stages accumulate in the human bone marrow. *Sci. Transl. Med*. **6** (2014).

38. M. De Niz, *et al., Plasmodium* gametocytes display homing and vascular transmigration in the host bone marrow. *Sci. Adv*. **4** (2018).

39. N. Obaldia, *et al.*, Bone marrow is a major parasite reservoir in *Plasmodium vivax* infection. *MBio* **9**, 625–643 (2018).

40. B. Malleret, *et al.*, *Plasmodium vivax*: Restricted tropism and rapid remodeling of CD71-positive reticulocytes. *Blood* **125**, 1314–1324 (2015).

41. K. Venugopal, F. Hentzschel, G. Valkiūnas, M. Marti, *Plasmodium* asexual growth and sexual development in the haematopoietic niche of the host. *Nat. Rev. Microbiol.* **18**, 177–189 (2020).

42. C. Zhang, The role of inflammatory cytokines in endothelial dysfunction. *Basic Res. Cardiol.* **103**, 398 (2008).

43. G. N. McKay, N. Mohan, N. J. Durr, Imaging human blood cells in vivo with oblique back-illumination capillaroscopy. *arXiv* **11**, 2373 (2020).

44. S. N. Kariuki, *et al*., Red blood cell tension protects against severe malaria in the Dantu blood group. *Nature* **585**, 579–583 (2020).

45. C. Lim, *et al.,* Expansion of host cellular niche can drive adaptation of a zoonotic malaria parasite to humans. *Nat. Commun*. **4**, 1–9 (2013).

46. R. W. Moon, *et al*., Normocyte-binding protein required for human erythrocyte invasion by the zoonotic malaria parasite *Plasmodium knowlesi*. *Proc. Natl. Acad. Sci. U. S. A.* **113**, 7231–7236 (2016).

47. W. H. Tham, J. Healer, A. F. Cowman, Erythrocyte and reticulocyte binding-like proteins of *Plasmodium falciparum*. *Trends Parasitol*. **28**, 23–30 (2012).

48. S. P. Wertheimer, J. W. Barnwell, *Plasmodium vivax* interaction with the human Duffy blood group glycoprotein: Identification of a parasite receptor-like protein. *Exp. Parasitol.* **69**, 340–350 (1989).

49. L. J. Chan, M. H. Dietrich, W. Nguitragool, W. H. Tham, *Plasmodium vivax* Reticulocyte Binding Proteins for invasion into reticulocytes. *Cell. Microbiol.* **22** (2020).

50. A. V. Hoffbrand, P. A. H Moss, *Essential Haemotology,* 6th Ed, Wiley and Blackwel (2011)

51. S. Dasgupta *et al.*, Membrane-wrapping contributions to malaria parasite invasion of the human erythrocyte. *Biophys. J.* **107**, 43–54 (2014).

52. M. L. Jones, C. Cottingham, & J. C. Rayner, Effects of calcium signaling on *Plasmodium falciparum* erythrocyte invasion and post-translational modification of gliding-associated protein 45 (PfGAP45). *Mol. Biochem. Parasitol.* **168**, 55–62 (2009).

53. H. M. Kudyba, D. W. Cobb, J. Vega-Rodríguez, V. Muralidharan, Some conditions apply: Systems for studying *Plasmodium falciparum* protein function. *PLOS Pathog*. **17**, e1009442 (2021).

54. L. E. Boucher, J. Bosch, The apicomplexan glideosome and adhesins — structures and function. *J. Struct. Biol*. **190**, 93–114 (2015).

55. D. Y. Bargieri *et al*., *Plasmodium* merozoite TRAP family protein is essential for vacuole membrane disruption and gamete egress from erythrocytes. *Cell Host Microbe* **20**, 618–630 (2016).

56. M. Zhang, *et al.,* Uncovering the essential genes of the human malaria parasite *Plasmodium falciparum* by saturation mutagenesis. *Science* **360**, eaap7847 (2018).

57. E. Knuepfer, et al., Divergent roles for the RH5 complex components, CyRPA and RIPR in human-infective malaria parasites. *PLOS Pathog*. **15**, e1007809 (2019).

58. H. Fang *et al.,* Epistasis studies reveal redundancy among calcium-dependent protein kinases in motility and invasion of malaria parasites. *Nat Commun*. **9**(1):4248 (2018).

59. W. Trager, J. B. Jensen, Human malaria parasites in continuous culture. *Science* **193**, 673–675 (1976).

60. M. Tibúrcio *et al.,* A novel tool for the generation of conditional knockouts to study gene function across the *Plasmodium falciparum* life cycle. *mBio* **10**(5) (2019).

61. F. Mohring *et al*., Rapid and iterative genome editing in the malaria parasite *Plasmodium knowlesi* provides new tools for *P. vivax* research. *eLife* **8**, e45829 (2019).

62. M. L. Jones *et al.* A versatile strategy for rapid conditional genome engineering using loxP sites in a small synthetic intron in *Plasmodium falciparum*. *Sci. Rep.* **6**, 21800 (2016).

63. T. Ishino *et al.*, Rhoptry neck protein 2 expressed in *Plasmodium* sporozoites plays a crucial role during invasion of mosquito salivary glands. *Cell. Microbiol.* **21** (2019).

64. T. Endo, H. Tokuda, K. Yagita, T. Koyama, Effects of extracellular potassium on acid release and motility initiation in *Toxoplasma gondii*. *J. Protozool.* **34**, 291–295 (1987).

Acknowledgements

The authors thank Sujaan Das and Markus Meissner (supplying *P. falciparum* ACT1), Abigail Perrin and Michael Blackman (supplying *P. falciparum* GAP45:loxP), Alex Hunt (maintaining *T. gondii*), Nattawat Chaiyawong and Edwin Too (maintaining *P. yoelii*). We also thank Reiko Tanaka, Nana Matsumoto, and Momoko Sakura for technical assistance. We are grateful to Japanese Red Cross Blood Society and UK NHS Blood and Transfusion Service for providing human erythrocyte and plasma. This study was conducted at the Joint Usage/Research Center on Tropical Disease, Institute of Tropical Medicine, Nagasaki University, Japan and London School of Hygiene and Tropical Medicine, UK. This work was supported by Fund for the Promotion of Joint International Research, Fostering Joint International Research, 16KK0183 (KY), 19KK0201 (KY), MEXT, Japan. This work was also supported in part by the Grants-in-Aids for Scientific Research, 15K08448 (KY), 19K07525 (KY), 16H05184 (OK), and 19H03461 (OK), MEXT, Japan. RWM was supported by a UK Medical Research Council Career Development Award (MR/M021157/1) and MNH was supported by a Bloomsbury Colleges Studentship. HD and MT receive funding from The Francis Crick Institute, which receives its core funding from Cancer Research UK (FC001189), the UK Medical Research Council (FC001189), and the Wellcome Trust (FC001189). The funders had no role in study design, data collection and analysis, decision to publish, or preparation of the manuscript.

Author Contributions

KY, MNH, RWM, SCW, MA, MT, and OK conceived and designed research. KY and MNH performed research. HD contributed the generation of transgenic parasite lines. SCW and MNH designed and performed the endothelial surface gliding assays. KY,

MNH, TT, MT, RWM, and OK wrote the paper, and all authors contributed to the manuscript and analyzed the data.

Declaration of Interests

The authors declare no competing interests.

Data and materials availability

All data are available in the manuscript.

Figure 1

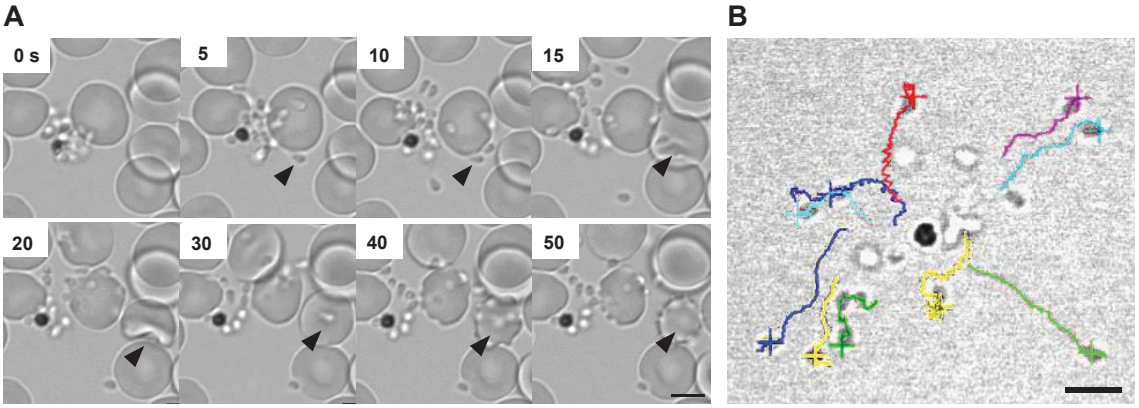

Fig. 1. Gliding motility of *P. falciparum* merozoites. (*A***)** Time-lapse imaging for *P. falciparum* merozoite gliding motility and erythrocyte invasion. Still images from Movie S1. Arrowhead indicates a merozoite gliding on the coverslip (5 and 10 seconds), followed by erythrocyte deformation (15 and 20 seconds) and merozoite internalisation (30–50 seconds). (*B*) Each merozoite was traced in different colors and gliding speed was evaluated from Movie S2.

Figure 2

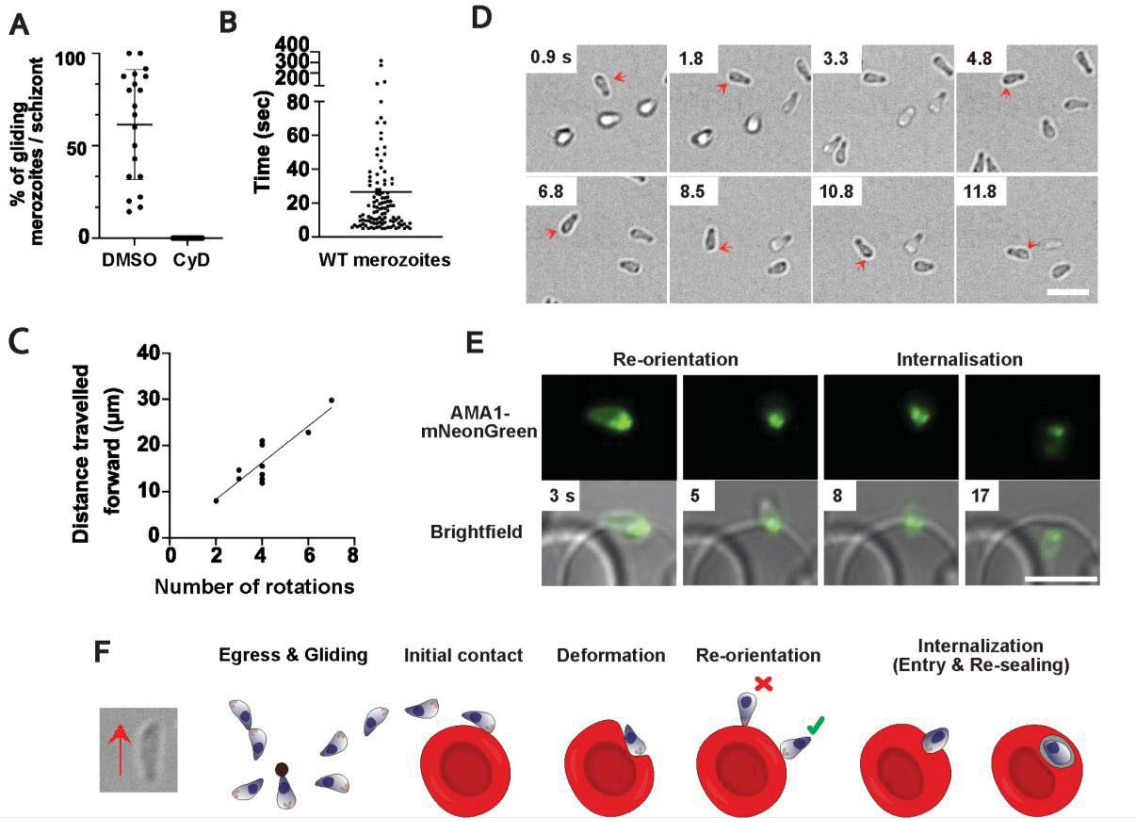

Fig. 2. Gliding motility of *P. knowlesi* merozoites. (*A*) The percentage of merozoites within a *P. knowlesi* schizont which exhibit motility, both for DMSO-treated parasites (mean = 62.5%) and 0.1 µM Cytochalasin D (CyD; IC_{50} = 0.023 ± 6.7 nM) -treated parasites (no gliding observed). A 'motile' merozoite was defined as having demonstrated directional forward motion along the surface of the coverslip for at least 5 continuous seconds. Each dot is representative of one schizont (n = 20). Error bars denote +/- 1 SD (*B*) The total time each motile *P. knowlesi* merozoite (n = 109; median = 15 seconds) spent gliding during the 10-minute imaging window post-egress. Error bars indicate interquartile range. (*C*) Number of rotations that merozoites completed plotted against the distance travelled for each glide (n = 10). As the number of rotations increased, so did the distance travelled forward, indicating rotation drives forward motion (Pearson correlation coefficient, R = 0.88). (*D*) Time lapse imaging demonstrating a *P. knowlesi* merozoite rotating as it glides. Red arrows indicate a dark spot located to one side of the wider end of the merozoite, which shifts to the opposite side (shown in subsequent frames), as it turns, and then back to the original position to complete a full rotation (see Movie S6). Scale bar represents 5 µm. (*E*) Time lapse imaging depicting a *P. knowlesi* merozoite with mNeonGreen-tagged AMA1 invading an erythrocyte. Panels 1 and 2 demonstrate re-orientation of the wider end of the

797 merozoite to align with the erythrocyte membrane. This is followed by the formation of
798 the moving junction, depicted as two green dots at the merozoite-erythrocyte interface
799 (panel 3), and finally entry into the host cell (panel 4). Scale bar represents 5 µm. (*F*)
800 Schematic illustrating gliding and erythrocyte invasion. Gliding proceeds with the wider,
801 apical end of the merozoite leading. During gliding, merozoites stretch, and a pointed
802 protrusion can be seen at the wider end of the zoite (left hand brightfield image), which
803 engages with the erythrocyte membrane upon re-orientation and internalisation. Re-
804 orientation of the zoite to make a contact of wider end (green tick), and not the thinner
805 end of the zoite as previously hypothesized (red cross), with the erythrocyte
806 membrane occurs prior to entry. During internalisation, constriction of the apical end
807 of the zoite causes the basal end to expand. Finally, after entry is complete, the
808 parasite resides in a parasitophorous vacuole where its development continues.

809

Figure 3

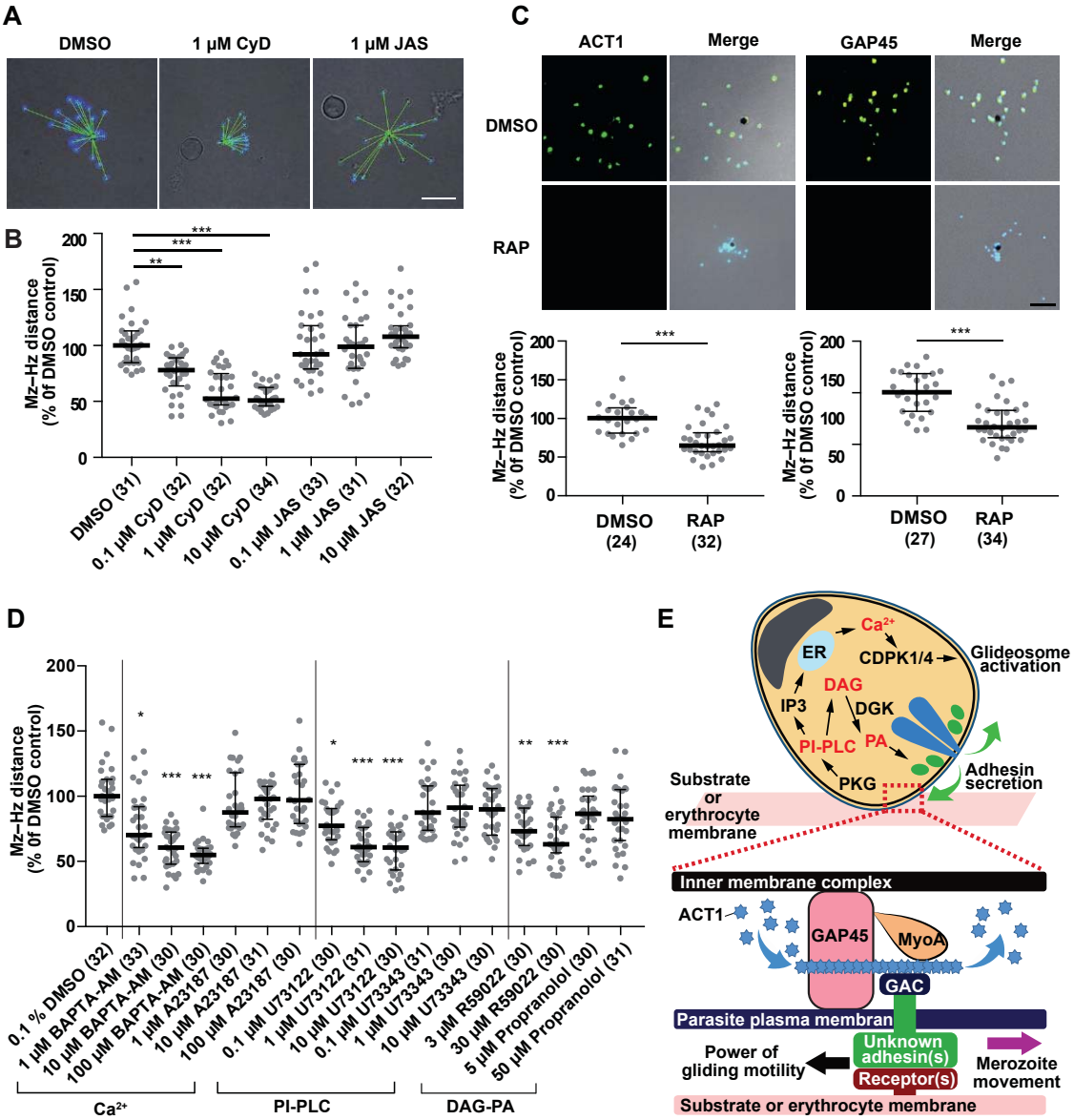

Fig. 3. The effects of chemical compounds and parasite genetic modifications on *P. falciparum* merozoite gliding motility. Purified *P. falciparum* schizonts were seeded on the coverslip and merozoites were left to egress for 1 hour. (*A*) The distance of the merozoite nucleus (DAPI, Mz) from hemozoin (black pigment, Hz) was measured (green line, Mz–Hz distance). Where indicated in the y-axes (panels *B* and *C*) the relative Mz–Hz distance compared to DMSO control obtained from each schizont with their median and interquartile range are shown. The number of analyzed schizonts from three independent experiments are indicated in the parentheses. (*B*) Effect of 0.1% DMSO, 0.1, 1, or 10 μM cytochalasin D (CyD, IC_{50} = 0.085 ± 0.029 μM, or jasplakinolide (JAS, IC_{50} = 0.110 ± 0.019 μM) were evaluated for merozoite gliding motility. **, and *** indicate $p < 0.001$, and < 0.0001, respectively. (*C*) Inhibition of gliding motility in rapamycin (RAP)-treated ACT1- or GAP45-deleted *P. falciparum* parasites. IFA with specific antibodies indicated ACT1 or GAP45 were not detected in

824 RAP-treated transgenic parasites. *** indicates $p < 0.0001$ by the Mann-Whitney test.
825 (*D*) Purified *P. falciparum* schizonts were treated with BAPTA-AM (IC_{50} = 0.992 ± 0.187
826 μM), A23187 (IC_{50} = 0.588 ± 0.029 μM), U73122 (IC_{50} = 0.271 ± 0.085 μM), U73343
827 (IC_{50} = 5.444 ± 0.199 μM), R59022 (IC_{50} = 4.678 ± 0.392 μM), or propranolol (IC_{50} =
828 0.551 ± 0.135 μM) and merozoite gliding assays were performed. The relative Mz–Hz
829 distance compared to DMSO control obtained from each schizont with their median
830 and interquartile range are shown. The number of analyzed schizonts from three
831 independent experiments are indicated in the parentheses. *, **, and *** indicate $p <$
832 0.05, < 0.001, and < 0.0001, respectively. (*E*) Overview of molecular mechanisms for
833 gliding motility of *P. falciparum* merozoite. After merozoite egress from the erythrocyte,
834 merozoite adhesin(s) are secreted from micronemes (green) via a signaling pathway
835 involving phosphoinositide-phospholipase (PI-PLC) and diacylglycerol (DAG) kinase
836 (DGK) and bind to environmental substrates including the erythrocyte membrane. A
837 pathway involving PI-PLC and Ca^{2+} activates calcium dependent protein kinases
838 (CDPKs) and phosphorylates the components of the glideosome machinery (32-35,
839 58). Grey, nucleus and blue, rhoptries. Gliding motility is powered by an actomyosin
840 motor of the glideosome machinery and the merozoite movement is transferred to the
841 erythrocyte membrane causing erythrocyte deformation upon merozoite attachment.
842 ACT1, actin-1; IMC, inner membrane complex; PKG, cyclic GMP-dependent protein
843 kinase; PA, phosphatidic acid; GAP45, glideosome-associated protein 45; MyoA,
844 myosin-A; and GAC, glideosome-associated connector.
845

Figure 4

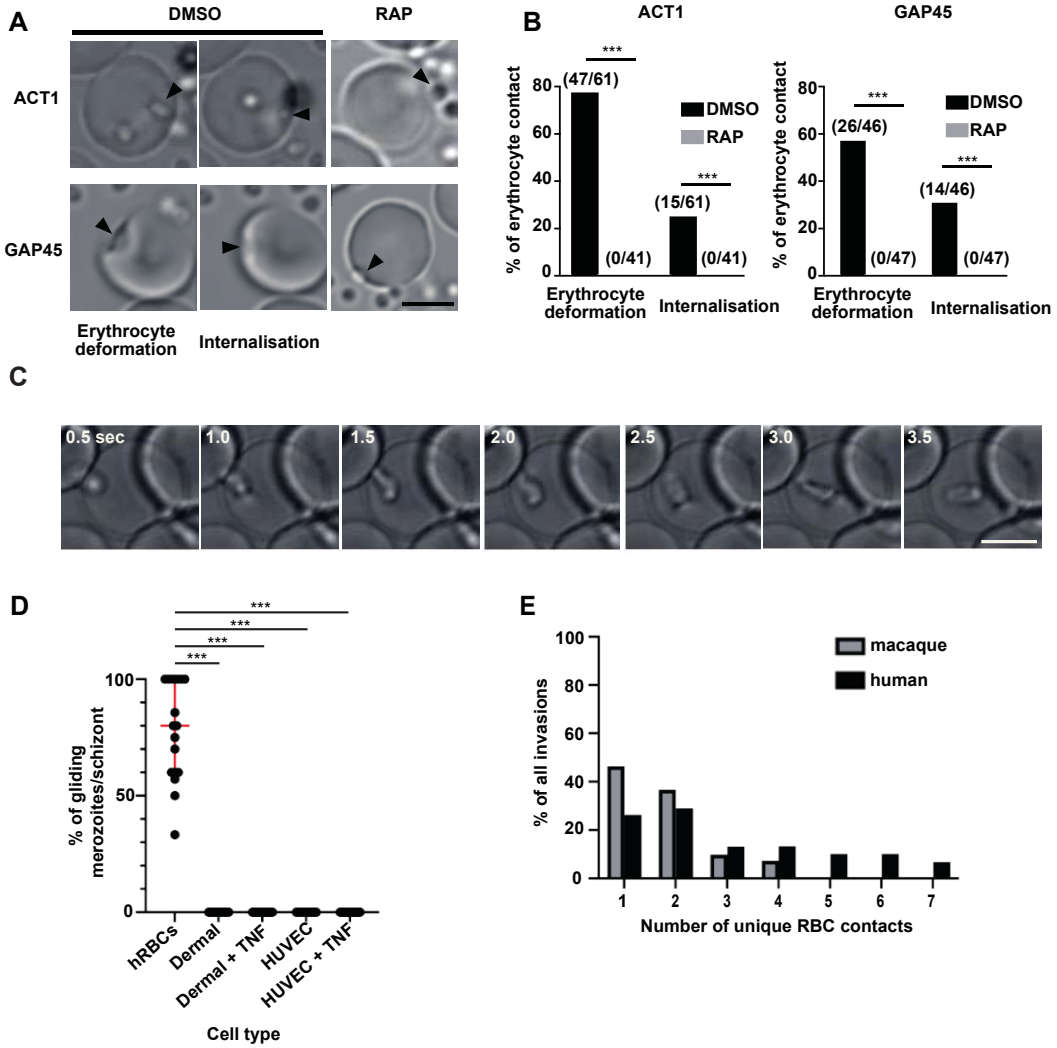

Fig. 4. A role for gliding motility in facilitating merozoite-erythrocyte interactions. (*A* and *B*) Erythrocyte deformation and merozoite internalisation events were seen for DMSO-treated ACT1- or GAP45-floxed *P. falciparum* parasites, but not detected after RAP-treatment ($p < 0.001$ for all by two-tailed Fisher's exact test). Scale bar represents 5 µm. (*C*) Still images taken from Movie S7, depicting a *P. knowlesi* merozoite beginning to deform a human erythrocyte as gliding motility is initiated along the surface of the host cell. Scale bar represents 5 µm. (*D*) A median 80% of merozoites within a given schizont demonstrate gliding motility along human erythrocytes (n = 18 schizonts). In contrast, no gliding is observed at all on either TNF stimulated or non-stimulated HUVEC (n = 16 and 10 schizonts, respectively) and dermal endothelial cells (n = 16 and 10 schizonts, respectively). Comparisons were made by one-way ANOVA, using a Kruskal-Wallis test; *** indicates $p<0.0001$. (*E*) The total number of unique erythrocyte contacts each invading merozoite made was significantly lower for macaque (n = 41 invasions) vs human (n = 38 invasions) erythrocyte invasions. Comparisons were made using Poisson regression (Poisson coef. 0.076, 95% CI - 0.37 - 0.52; $P<0.001$).

Supplemental Information

Gliding motility of *Plasmodium* merozoites

Kazuhide Yahata*, Melissa N. Hart, Heledd Davies, Masahito Asada, Samuel C. Wassmer, Thomas J. Templeton, Moritz Treeck, Robert W. Moon*, Osamu Kaneko

*Correspondence: kyahata@nagasaki-u.ac.jp or rob.moon@lshtm.ac.uk

This PDF file includes:

- Figures S1 to S4
- Tables S1
- Legends for Movies S1 to S10

Other supplementary materials for this manuscript include the following:

- Movies S1 to S10

Supplementary Figures

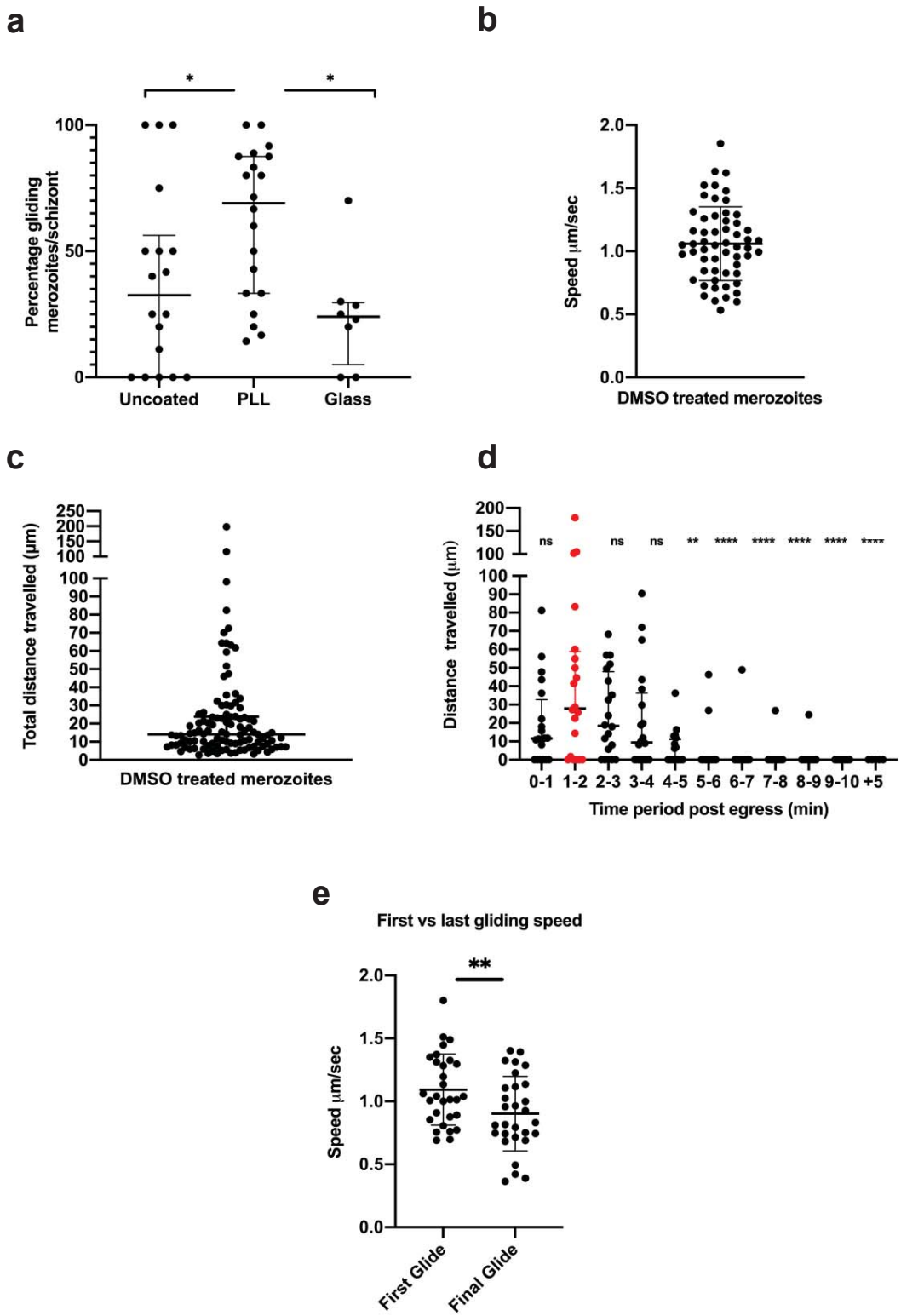

Fig. S1. *Plasmodium knowlesi* merozoite gliding speed and duration. a, merozoite motility on different surfaces. The percentage of merozoites exhibiting motility decreases from 62% on poly-L-lysine surfaces (n = 20 schizonts) to 38% on uncoated surfaces (n = 18 schizonts; * $p < 0.05$) and 25% on glass surfaces (n = 8; *

$p < 0.02$). Means compared using one-way ANOVA and Dunnett's multiple comparison test**.** Error bars denote +/- 1 s.d. **b,** Speeds of individual merozoites (average = 1.06 µm/second; n = 57 merozoites). Error bars denote +/- 1 s.d. **c**, Total distance travelled by each merozoite. Merozoites travelled a median distance of 14 µm during the 10-minute window of imaging (minimum = 2.8 µm, maximum = 198.6 µm; n = 109 merozoites). **d**, Distances travelled by schizonts (a total of distances travelled by each merozoite) during each minute post egress (n = 20 schizonts) as well as after a 5-minute incubation in the dark (post egress) prior to commencing filming for 3 further minutes (designated as "+5"; n = 5 schizonts). The majority of gliding occurred within 5 minutes post egress, with peak gliding (median of 28 µm travelled) occurring 1-2 minutes post egress (** $p < 0.01$, **** $p < 0.0001$, and ns, not significant, as determined by a Kruskal-Wallis test). This delay is likely due to a small 'settling period' during the first 60 seconds, while merozoites disperse and begin to connect to the slide coverslip. Error bars denote interquartile range. **e**, First vs last gliding speeds. Comparison by two-tailed paired t-test between the speed of the first and final glides of merozoites (** $p < 0.005$; n = 29) shows that gliding speed decreases from 1.09 µm/second (average first glide) to 0.90 µm/second (average last glide), indicative of decreasing gliding efficiency over time. Error bars denote +/- 1 s.d.

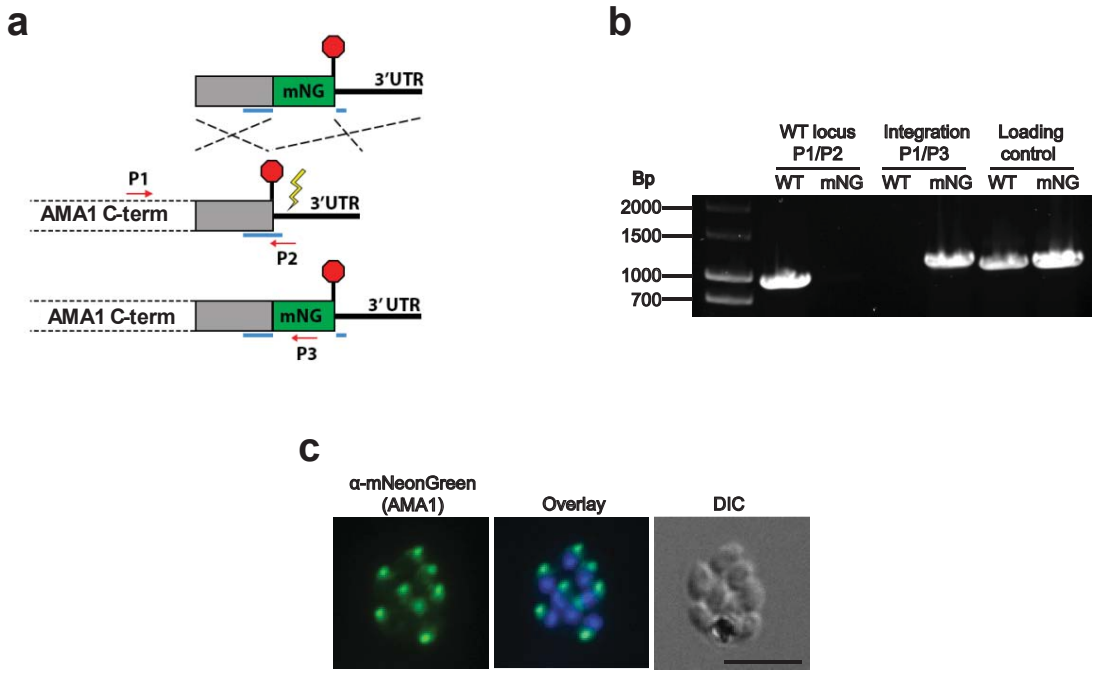

Fig. S2. Generation of *Plasmodium knowlesi* parasites with mNeonGreen-tagged AMA1. a, Schematic depicting integration of mNeonGreen (mNG)-tagging construct into the *AMA1* locus. Donor DNA was synthesized by overlapping PCR, and consisted of the mNG sequence flanked by 500 bp homologous regions to the C-terminus and 3'UTR of the *AMA1* locus. A sgRNA (position underlined in blue) targeted a CRISPR-Cas9-induced double stranded break (yellow lightning) immediately after the stop codon. Upon repair, the guide sequence was split in two by the insertion of the tag, ablating further Cas9 activity. Positions of diagnostic primers were indicated by red arrows. **b**, Diagnostic PCR showing the absence of wild type (WT) parasites (primers P1/P2; expected band size 988 bp), and the presence of transgenic parasites (mNG; primers P1/P3; expected band size 1118 bp) in the transfected line, along with control PCR reaction detecting unrelated locus. Primers for PCR were listed in Table S1. **c**, Indirect immunofluorescence assay detecting the AMA1-mNeonGreen fusion protein. Antibody specific for the mNeonGreen tag detects the protein expressed in late stage schizonts, which are localised to the apical end of merozoites. Scale bar indicates 5 μm.

Supplementary Figure 2

a

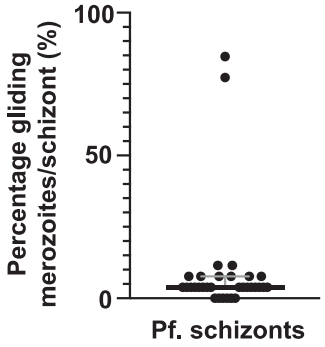

b

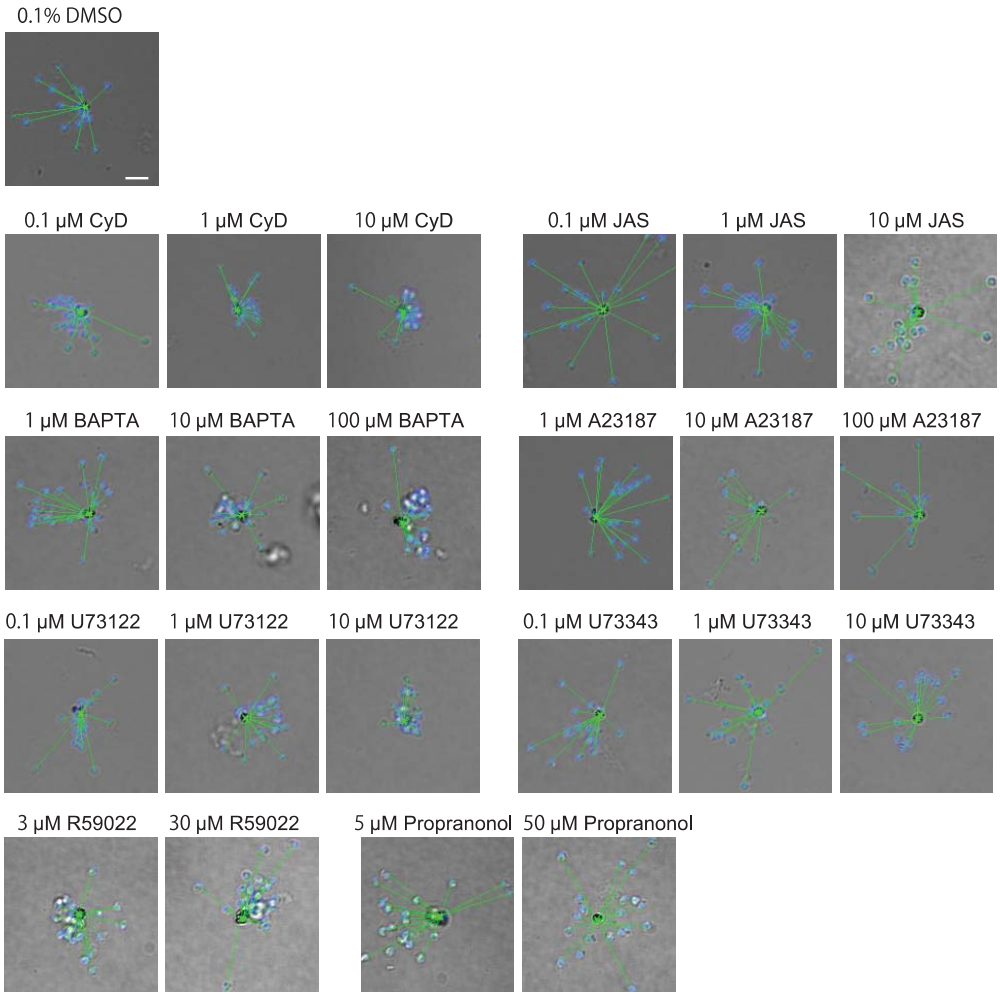

Fig. S3. *Plasmodium falciparum* merozoite gliding assay with a panel of chemical compounds. a, The percentage of *P. falciparum* merozoites exhibiting motility (n = 32 schizonts). The median (3.85%) and interquartile range are shown. **b**, Compound-treated merozoites were allowed to egress and fixed. The distance between merozoite DNA stained with Hoechst33342 (blue) and hemozoin were measured (green line). Cytochalasin D (CyD), jasplakinolide (JAS), BAPTA-AM (BAPTA), A23187, U73122, U73343, R59022, and propranolol were used in this assay. Scale bar represents 5 μm.

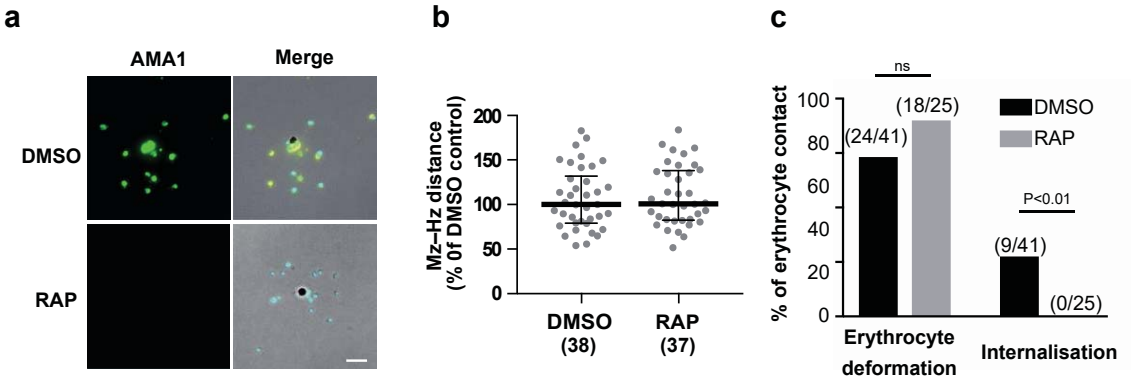

Fig. S4. Effect of AMA1-deletion for *Plasmodium falciparum* merozoite gliding motility, erythrocyte deformation, and merozoite internalisation. **a**, PfAMA1:loxP parasite line was treated with DMSO or rapamycin (RAP) and merozoites egressed from infected erythrocytes were stained with anti-AMA1 antibody (green). Right panels, merged images of green AMA1 signals, blue nucleus signals, and differential interference contrast images. **b**, The merozoite (Mz)-hemozoin (Hz) distances (median and interquartile range) were obtained from two biological replicates. No statistically significant difference was detected between DMSO- and RAP-treated parasites by two-tailed Fisher's exact test. **c**, The number of erythrocyte deformation events was not different between DMSO- and RAP-treated parasites. However, merozoite internalisation events seen for DMSO-treated parasites were not detected in RAP-treated AMA1-deleted parasites ($p < 0.01$ by two-tailed Fisher's exact test). ns, not significant. Scale bar represents 5 μm.

97 **Supplementary Table**

98 **Table S1:** Primers for PCR to generate *Plasmodium knowlesi* parasite with

99 mNeonGreen-tagged AMA1.

Primer name	Primer number	Sequence
AMA-1_Diagnostic_Fwd	P1	CCACAAAATTTACACAATTAATTATTGTTGCTGC
AMA-1_Diagnostic_WT_rev	P2	GCTTCCCCACTCAGTAGTAAGG
AMA1_Diagnostic_Integration_rev	P3	TTGGATTTCCTGTTCCTTGTCCAACC
Diagnostic_control_Fwd	P4	CCCGGGGCGTTTTCGCGTATCTGCGCTTTTTC
Diagnostic_control_Rev	P5	CCTAGGGGACAATATATCCTCACAGAACAACTTG
AMA-1_HR1_Fwd	P6	CAACCGAATCGTTTTCGAAGCTAG
AMA-1_HR1_Rev	P7	ACCTCCGCTGCCTCCACCGGATCCGTAGTAAGGCTTCTCCATCAGAACAG
AMA-1_HR2_Fwd	P8	GGGAATGGATGAATTGTATAAATAATGAGTGGGGAAGCAACGTATTATTCG
AMA-1_HR2_Rev	P9	TATGGATTATATTAAAGTAAGCGTATACGCCATG
mNeonGreen_Fwd	P10	GGATCCGGTGGAGGCAGCGG
mNeonGreen_Rev	P11	CGACAGGTTTCCCGACTGGAAAG
HR1/mNeonGreen_Fusion_Fwd	P12	TGATTAAAAGTGCCTTTCTTCCAGTGG
HR1/mNeonGreen_Fusion_Rev	P13	TTATTTATACAATTCATCCATTCCCATAACATCTGT
HR1/mNeonGreen/HR2_Fusion_Rev	P15	TAGAGTGCTCATATAAGGCACGCAC

100

101

Supplementary Movies

Movie S1 (separate file). *Plasmodium falciparum* merozoite gliding motility and erythrocyte invasion on an ibiTreat coverslip (5 frames/second).

Movie S2 (separate file). Gliding motility of *Plasmodium falciparum* merozoites with 0.1% DMSO on an ibiTreat coverslip (10 frames/second).

Movie S3 (separate file). *Plasmodium knowlesi* merozoites treated with 0.005% DMSO gliding on a poly-L-lysine-coated coverslip (1 frame/second). Parasites were filmed immediately post egress.

Movie S4 (separate file). Egress of *Plasmodium knowlesi* merozoites from wheatgerm agglutinin-stained RBCs treated with 100 nM cytochalasin D on a poly-L-lysine-coated coverslip (1 frame/second).

Movie S5 (separate file). A *Plasmodium knowlesi* merozoite, designated by a red cross, demonstrating corkscrew-like rotation whilst travelling across a poly-L-lysine-coated coverslip (10 frames/second).

Movie S6 (separate file). A *Plasmodium knowlesi* merozoite with mNeonGreen-tagged AMA1 invading an erythrocyte via its ‘wide’ apical end (1 frame/second).

Movie S7 (separate file). *Plasmodium falciparum* merozoite gliding motility on an ibiTreat coverslip (10 frames/second). Filming commenced 4 minutes before egress. A red arrow shows merozoite gliding.

Movie S8 (separate file). A *Plasmodium knowlesi* merozoite deforming a human erythrocyte whilst gliding across its surface (10 frames/second).

Movie S9 (separate file). Egress of *Plasmodium knowlesi* merozoites on human dermal endothelial cells grown on fibronectin-coated μ-Slides (1 frame/second).

Movie S10 (separate file). *Plasmodium knowlesi* merozoites completing several short glides on the surface of erythrocytes on a poly-L-lysine-coated coverslip (1 frame/second). A red arrow appears at the beginning of each glide.